ChemPubSoc Europe

DOI: 10.1002/celc.201700511

CHEMELECTROCHEM Articles

Thermal Treatment Effects on Electrodeposited Sb_2Se_3 Photovoltaic Thin Films

Magno Barcelos Costa,[a] Francisco Willian de Souza Lucas,[a] and Lucia Helena Mascaro*[a]

Antimony selenide thin films were prepared through potentiostatic co-electrodeposition by applying −0.6 V from a bath composed of 2.5 mM $K(SbO)C_4H_4O_6 \cdot 0.5\ H_2O$ and 2.0 mM SeO_2 in a supporting electrolyte of 0.5 M Na_2SO_4/H_2SO_4 at pH 2. The films were subjected to different thermal treatment (TT) conditions under a $Se_{(vapor)}/N_2$ atmosphere. Cyclic voltammetry was used to evaluate the electrochemical process of each element separately as well as the binary system on Pt and FTO working electrodes. The morphology, composition, band gap, crystallography, and photoactivity toward hydrogen gas production of the films were evaluated as a function of TT conditions, in order to obtain insight into their effects on film properties. Under all conditions, the films showed homogeneous and rough surfaces and a stoichiometric Sb_2Se_3 composition. The non-thermal-treated film was non-crystalline, whereas after TT, all films showed a pure orthorhombic Sb_2Se_3 phase. It was observed that the crystallographic texturization of films in the (120) plane, caused by some TT conditions, is detrimental to the photoactivity. At the optimized TT conditions (300 °C for 3 h), the film presented good crystallographic and optoelectronic properties and photoactivity, with a photocurrent value of 168.15 μA cm^{-2} (at the standard hydrogen gas evolution potential) and a band gap of around 1.1 eV.

1. Introduction

In recent decades, unfavorable prospects for the depletion of petroleum-based energy resources have raised concerns. The increase and volatility in prices, and the serious effects caused to the environment, have contributed to the pursuit of technology that could potentially replace these energy sources, favoring the use of renewable resources. Given these circumstances, the sun is seen as an inexhaustible source of energy, with it being one of the most promising and clean alternatives among those currently existing.[1] Thus, the photovoltaic (PV) conversion of sunlight into electricity, using semiconductor-based devices, is highlighted by providing a secure, viable and non-destructive way of harvesting solar energy and providing up to the 30 terawatts of carbon-free power required by the mid-21st century.[2–4]

Among the different kinds of PV devices, thin film-based PV (TFPV) devices are promising technologies for further decreasing current costs and addressing the economic scalability of Si-based solar cells that dominate the market.[5] Some of the most studied TFPV technologies include $Cu(In,Ga)Se_2$[6,7] (CIGS, 22.6% energy conversion efficiency[8]) and CdTe[9] (22.1% efficiency[8]). However, the scarcity of raw materials (In and Ga) and elemental toxicity (Cd) may limit the environmental benefits and potential terawatt scaling of these solar cell technologies.[10] Thus, emerging light absorber materials with less toxic and more abundant elements are of increasing interest. On this basis, $Cu_2ZnSn(Se,S)_4$ (CZTSSe) is the most promising material in terms of the reported PV conversion efficiency (certified 12.6%),[8,11] but its chemical complexity may hinder further improvements. These considerations have led to a resurgent interest in less complex, non-toxic earth-abundant absorbers, such as $Cu_3P(S,Se)_4$,[12] Cu_2SnS_3,[13,14] $CuSbS_2$[15–18] and Sb_2Se_3.[19–21]

Recently, several groups[19–21] have reported studies on Sb_2Se_3 as an alternative material for TFPV devices, because it presents excellent photovoltaic properties, with a direct and indirect band gap in a range from 1.0 to 1.2 eV[22,23] that falls within the optimum range for a single junction terrestrial solar cell,[21,24] a high absorption coefficient of $>10^5$ cm^{-1} at 1.2 eV that is slightly better than those of CIGSe and CZTSSe, and a melting point of 611 °C,[25] amenable to grain growth at relatively low temperatures. Added to these properties, Sb_2Se_3 has earth-abundant and low toxic elements,[26] and low structural complexity, presenting only a single crystallographic phase.[27] In Sb_2Se_3, each Sb and Se atom is linked to three oppositely charged atoms, with the orthorhombic unit cells forming one-dimensional $(Sb_4Se_6)_n$ ribbon structures that are linked by van der Waals forces.[28]

Since vacuum-based growth processes are often not desirable for the production of low-cost technologies, in order to reduce costs, non-vacuum methods have been pursued worldwide by researchers and, among theses, electrodeposition has been highlighted. Electrodeposition is a simple, fast and economical process that is able to produce good quality semiconductor films on different kinds of conducting substrates (with large and different geometries) and it can be conducted at low temperatures. Another attractive feature of this method is that the thickness and composition of the films can be controlled by deposition parameters, such as the supporting electrolyte, potential, current density and bath composition and temperature.[29] Several PV absorber semiconductors have been grown by electrodeposition, including CdTe,[30–32]

[a] M. B. Costa, Dr. F. W. de Souza Lucas, Prof. Dr. L. H. Mascaro
Federal University of São Carlos, Road Washington Luiz, km 235, São Carlos, SP 13565-905, Brazil
Tel.: +55 (016) 3351-8082
E-mail: lmascaro@ufscar.br

CIGSe,[33,34] CZTSe[35,36] and Sb_2Se_3[21] At the laboratory scale, electrodeposited CIGSe- and CZTSe-based PV devices have achieved efficiencies of over 10%[33,34,36] and 8%,[35,36] respectively.

In 2012, Lai and his group investigated the deposition mechanism of Sb_2Se_3 films by cyclic voltammetry (CV) onto thin oxide glass, showing the formation of a binary compound by a co-deposition mechanism.[37] Moreover, the effects of different deposition potentials on the structure, morphology and composition of the films were also studied, in which a Sb_2O_3 secondary phase was observed in one of the conditions. In the same year, the same group prepared and characterized Sb_2Se_3 thin films by varying other conditions, such as pH, potential and deposition temperature, followed by thermal treatment (TT) that was not systematically optimized.[25] The orthorhombic Sb_2Se_3 compound was demonstrated and a photocurrent density of 50 $\mu A\,cm^{-2}$ was achieved in 0.5 M H_2SO_4, under 100 $mW\,cm^{-2}$ of illumination and at a potential 260 mV more negative than the standard hydrogen reduction potential. As far as we know, there is no work in the literature regarding the systematic study of the effects of TT under a Se atmosphere on Sb_2Se_3 PV devices or their photoelectrochemical properties.

Based on the aforementioned perspectives, this work proposes the design of Sb_2Se_3 thin films by electrodeposition, a non-vacuum method, and presents a systematic study of the TT effects on these films in order to find conditions for improving their optoelectronic quality and photoactivity toward hydrogen gas production by water splitting.

Experimental Section

All chemicals were of analytical grade and used directly without further purification. The following reagents were used: Na_2SO_4 (Sigma-Aldrich, >99.9%), H_2SO_4 (Aldrich, 98%), $K(SbO)C_4H_4O_6\times0.5\,H_2O$ (Sigma-Aldrich, >99%), SeO_2 (Alfa Aesar, >99,4%) and selenium powder (Vetec, >99.9%).

Electrochemical experiments were carried out using a potentiostat/galvanostat (Autolab PGSTAT 302 N, Metrohm-Eco Chemie). A three-electrode configuration electrochemical cell was used with fluorine-doped tin oxide (FTO, 7 ohm/sq, MTI corporation) coated glass (geometric area of 0.8 cm^2) or a Pt-disc (geometric area of 0.1 cm^2) as the working electrode, a Pt-plate as an auxiliary and a $Ag/AgCl/Cl^-_{(sat.\ KCl)}$ as the reference electrode. Before its use, the FTO was ultrasonically cleaned with deionized water, ethanol, acetone and isopropanol for 5 min in each solvent, followed by immersion in a 0.5 $mol\,L^{-1}$ $KMnO_4$ solution for 1 h and washed alternately with 30% H_2O_2 and deionized water. Then, the FTO was hydrophilized for 1 h at 70 °C in a solution of H_2O/H_2O_2 (conc.)/NH_4OH (conc.), in a ratio of 5:1:1, respectively. Finally, it was rinsed with deionized water and dried in a N_2 gas stream.

CV was used to evaluate the electrochemical process of each element separately at the Pt and FTO working electrodes. In this study, 1.0 mM SeO_2 and $K(SbO)C_4H_4O_6$ solutions and their mixture in a ratio of 1:1 were used. The supporting electrolyte was made from a 0.5 M Na_2SO_4 solution with the pH adjusted to 2 by adding 0.01 M H_2SO_4. The solutions were previously deaerated with a stream of N_2 gas introduced into each solution for 3 min before a scan. The CVs were recorded at a scan rate of 50 $mV\,s^{-1}$, from 1.35 to −1.20 V vs. $Ag/AgCl/Cl^-_{(sat.\ KCl)}$ on Pt and from 1.25 to −1.5 V vs. $Ag/AgCl/Cl^-_{(sat.\ KCl)}$ on FTO, toward the cathodic direction. After that, the potential for electrodeposition of the films was chosen, −0.6 V, and the films were obtained under potentiostatic conditions using a bath composed of 2.0 mM SeO_2 and 2.5 mM SbO^+ and a total charge of 600 mC, maintaining the geometric area of 1 cm^2 (in order to grow films with thickness of 300–400 nm, which is the thickness commonly used in the literature[21,22]).

In an attempt to observe the effect of the TT, the films were annealed under a Se atmosphere at different temperatures (300, 400 and 500 °C) and times (1, 3 and 6 h), with a heating/cooling rate of 10 °C min^{-1}. Each film was placed into a lead borosilicate glass cylinder (sample cylinder, volume of 300 mL) with the partial pressure of the Se gas controlled by means of a crucible with 0.2 g selenium powder placed inside the tube that was sealed by the friction of the two parts that compose it. In this process, a tube furnace was used with a N_2 gas atmosphere maintained at 1 atm and a flow of 1 $mL\,min^{-1}$ through a bubbler filled with mineral oil (Figure 1). Moreover, a film was left without TT for comparative purposes.

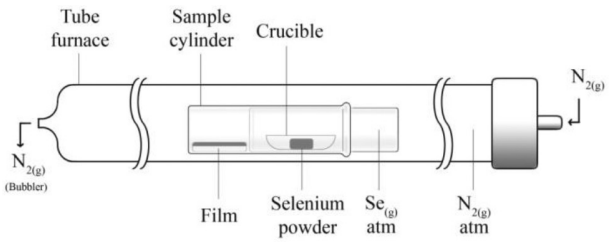

Figure 1. System used for the thermal treatments.

After their growth and TT, the morphology and composition of the films were evaluated by high-resolution field emission scanning electron microscopy (FE-SEM, Zeiss Supra 35) and energy dispersive X-ray (EDX) spectroscopy (FEI-SEM, Inspect S50 coupled to an Electron Back-Scattered Diffraction system, EBSD), respectively. In turn, their band gaps were determined by NIR-UV-vis spectroscopy with diffuse reflectance geometry, which was carried out in a Cary 5E® spectrometer from 1800 to 800 nm. The crystallographic characterization was performed with the aid of an X-ray diffractometer (Rigaku-DMax2500PC) with CuKα radiation, a scanning step of 0.02° and a counting time of 6 s.

For the photoelectrochemical experiments, an electrochemical cell with a quartz window (the optical path between the window and the film surface was 1 cm) was used. A supporting electrolyte composed of 0.5 M Na_2SO_4/H_2SO_4 at pH 2 was used, while a solar simulator with a 150 W xenon lamp (Newport 66902) acted as a light source and an AM 1.0 lens was used for simulating the sun light spectrum.

2. Results and Discussion

2.1. Electrochemical Behavior

The electrochemical behavior of the 1.0 mM H_2SeO_3 (from hydrolyzed SeO_2 hydrolyzed, Figure 2) and 1 mM SbO^+ (from hydrolyzed $KSbOC_4H_4O_6$, Figure 3) solutions, as well as their equimolar mixture (Figure 4), on Pt (geometric area of 0.1 cm^2) and FTO (geometric area of 0.8 cm^2) electrodes were studied by

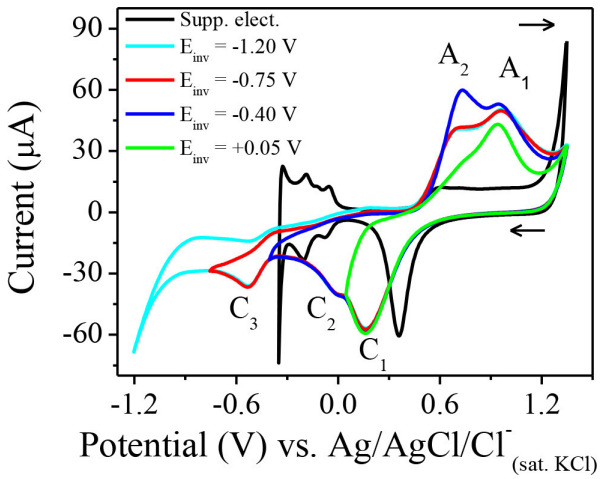

Figure 2. Cyclic voltammograms on Pt with different inversion potentials (E_{inv}) at a scan rate of 50 mV s^{-1}, for the solution constituted of 1.0 mM H_2SeO_3 in 0.5 M Na_2SO_4/H_2SO_4 at pH 2. The black line voltammogram shows the electrochemical profile of Pt in the supporting electrolyte.

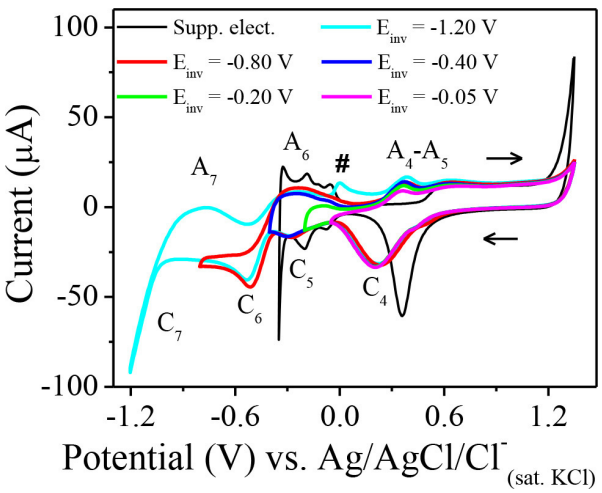

Figure 3. Cyclic voltammograms on Pt with different inversion potentials (E_{inv}) at a scan rate of 50 mV s^{-1}, for the solution containing 1.0 mM SbO^+ in 0.5 M Na_2SO_4/H_2SO_4 at pH 2. The black line voltammogram shows the electrochemical profile of Pt in the supporting electrolyte.

CV. The black line voltammograms show the electrochemical behavior of Pt (or FTO, in the case of Figure 4B) in the supporting electrolyte. On Pt, the hydrogen adsorption and desorption can be seen between 0 and −0.25 V, while the formation and reduction of PtO_x occur at 0.5 and 0.36 V, respectively. Figure 2 shows the first studied species, H_2SeO_3, displaying three cathodic and two anodic peaks.

In Figure 2, the C_1 and C_2 peaks at about 0.16 and 0.01 V can be associated with the reduction of Se^{4+} to Se^0 by underpotential deposition (UPD) and massive deposition, Eqs. (1) and (2), respectively. Santos and Machado[38] reported the same behavior in their microgravimetric and voltammetric studies of Se UPD on polycrystalline Pt. The C_3 peak (at about −0.5 V) can be correlated to the reduction of Se^0 to Se^{2-} via two electrons[39] or of Se^{4+} to Se^{2-} via six electrons,[37] as suggested in Eqs. (3) and (4), respectively.

$$H_2SeO_{3\,(aq)} + 4H^+_{(aq)} + 4e^- \rightleftharpoons Se_{(s,\ adatoms)} + 3H_2O_{(l)} \quad (1)$$

$$H_2SeO_{3\,(aq)} + 4H^+_{(aq)} + 4e^- \rightleftharpoons Se_{(s,bulk)} + 3H_2O_{(l)} \quad (2)$$

$$Se_{(s,bulk)} + 2H^+_{(aq)} + 2e^- \rightleftharpoons H_2Se_{(aq,g)} \quad (3)$$

$$H_2SeO_{3\,(aq)} + 6H^+_{(aq)} + 6e^- \rightleftharpoons H_2Se_{(aq,g)} + 3H_2O_{(l)} \quad (4)$$

From the voltammogram with an inversion potential (E_{inv}) at 0.05 V, we can conclude that the A_1 peak is associated with the C_1 peak, i.e., dissolution of the Se adatom layers. The small shoulder seen at the cathodic side of the A_1 peak is related to the A_2 peak that, in turn, is associated with Se bulk dissolution. For the CV with E_{inv} at −0.4 V, the increase of the A_2 peak is due to the increased quantity of Se bulk that was deposited during the direct scan. Discounting the contribution of the A_2 peak over the A_1 peak, we could find that the total charge of this last peak did not increase when the E_{inv} was more cathodic. This happened because this peak is surface limited. Finally, when the E_{inv} was more cathodic than the C_3 peak, there was a decrease in the A_2 peak intensity, since the associated process of forming Se^{2-} dissolves the Se film deposited during the direct scan.

For analysis of the SbO^+ electrochemical behavior, the E_{inv} values of −0.05, −0.20, −0.40 and −0.80 V were used in the studies on Pt (Figure 3), and the profile was compared to the one on FTO (Figure 4B).

According to Jung and coauthors,[40] two UPD peaks and one massive deposition may represent the reduction of the Sb^{3+} to Sb^0 on Pt. The same behavior was observed in our experiments, where these processes can be related to the C_4 (at 0.23 V), C_5 (at −0.26 V) and C_6 (at −0.51 V) peaks, respectively. These peaks are associated with Eqs. (5)–(7).[41]

$$SbO^+_{(aq)} + 2H^+_{(aq)} + 3e^- \rightleftharpoons Sb_{(s,1^{st}\ adatoms)} + H_2O_{(l)} \quad (5)$$

$$SbO^+_{(aq)} + 2H^+_{(aq)} + 3e^- \rightleftharpoons Sb_{(s,2^{nd}\ adatoms)} + H_2O_{(l)} \quad (6)$$

$$SbO^+_{(aq)} + 2H^+_{(aq)} + 3e^- \rightleftharpoons Sb_{(s,bulk)} + H_2O_{(l)} \quad (7)$$

The potential inversions at −0.05, −0.20 and −0.40 V show that the dissolution of the films grown by UPD is connected to the anodic peaks A_5–A_4. Likewise, the scan inversion at −0.80 V shows that the dissolution of the bulk Sb is associated to the broad A_6 peak. Now, when the E_{inv} is −1.2 V, we can see the C_7 process related to proton reduction or antimony hydride formation, with the redox couple at A_7. A new anodic peak "#" appeared for this E_{inv}, which can be associated with desorption of the hydrogen adatoms that were adsorbed on some exposed Pt area.

From the green line voltammogram of Figure 4A, we can observe a R_1 peak at the same potential of the Se and Sb 1st adatom UPDs, which means that in this region, the Sb and Se adatoms can react in the solid state to form Sb_2Se_3 (Equation (8)), as also observed by Chen et al.[41] on a gold surface.

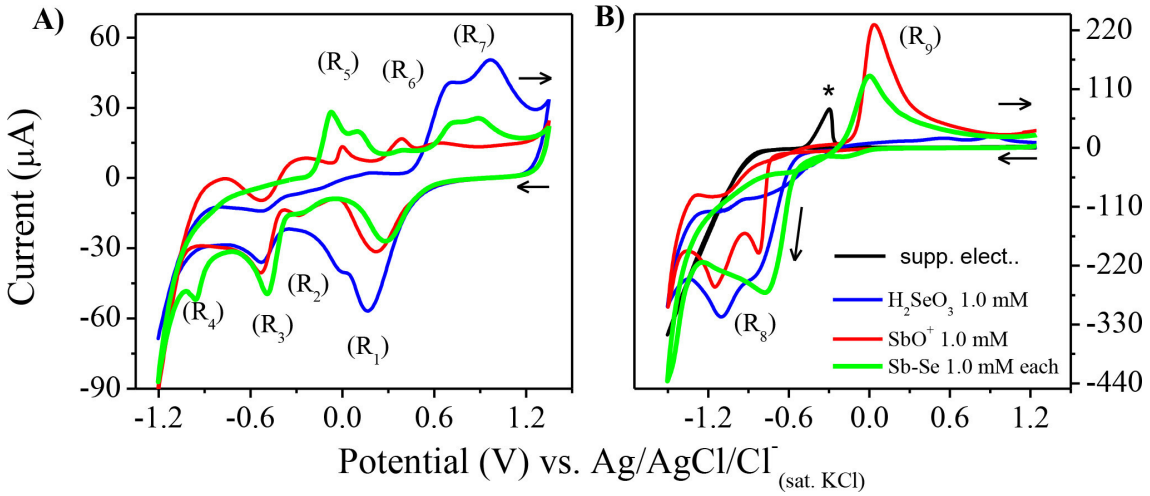

Figure 4. Cyclic voltammograms on A) Pt or B) FTO at a scan rate of 50 mV s^{-1}, and for the solutions containing 1.0 mM H_2SeO_3 (blue line), 1.0 mM SbO^+ (red line), and their equimolar mixture (green line) in 0.5 M Na_2SO_4/H_2SO_4 at pH 2.

The presence of this semiconductor Sb_2Se_3 layer on Pt explains the fact that the bulk Se (C_2) deposition dislocates to R_3 and the formation of selenide (C_3) shifts to R_4. The potential displacements of these processes were probed by the studies of E_{inv} (not shown here). Alternatively, the Sb 2st adatoms seem to not be affected by the Sb and Se adatoms present on the electrode, as seen in R_2. Since R_4 is related to H_2Se evolution (reactions associated with Eqs. (3) and (4)), this region is also related to the deposition of the Sb_2Se_3 film, following Eq. (9), and the peaks at R_5, that appear only when the E_{inv} is more negative than the peak at R_4 (the study of E_{inv} is not shown here), can be associated with the dissolution of Sb_2Se_3 and metallic Sb. The suppression of the Sb bulk and adatom dissolution (peaks at R_6) is evidence that these layers reacted in the solid state with Se to form Sb_2Se_3.

For the FTO electrode (Figure 4B curve black), there are no hydrogen adsorption and desorption processes, as was observed for Pt. In the reverse scan, we can see the anodic peak associated with the re-oxidation of FTO (*). In the blue line voltammogram that represents the H_2SeO_3 electrochemical behavior, as expected, there are no peaks related to Se adatoms deposition/dissolution, and the C_2 and C_3 peaks are shifted by ~700 and ~500 mV toward more negative potentials in relation to those observed on Pt (Figure 2), respectively. These shifts can be associated to the higher resistance of FTO compared to Pt. In sequence, the red line voltammogram shows the electrochemical behavior of SbO^+, the Sb bulk deposition seems to be split into two peaks; the C_6' can be related to the deposition of the first Sb bulk layers and the C_6'' represents the bulk deposition on this first formed Sb film. The peak shifts compared to those observed on Pt are associated with the higher resistance of FTO, as was also observed in the previous study. Finally, in the green line voltammogram, we can see the behavior of the binary system on FTO. Compared to the previous electrochemical behaviors on Pt and on FTO, we can argue that the peak at R_8 represents the simultaneous Se and Sb bulk deposition, which can be followed by the solid-state formation of Sb_2Se_3 film, according to the reaction shown in Eq. (10).[42] The peak at R_9 is only associated with the dissolution of excess metallic Sb that did not react with the elemental Se. From Figure 4B, a potential of −0.6 V was chosen for growing the Sb_2Se_3 film, a region where the growth is controlled by activation, instead of diffusion, and a better composition control is achieved.

$$3Se_{(s,\ adatoms)} + 2Sb_{(s,\ adatoms)} \rightleftharpoons Sb_2Se_{3(s)} \quad (8)$$

$$3H_2Se_{(aq,\ g)} + 2SbO^+_{(aq)} \rightleftharpoons Sb_2Se_{3(s)} + 2H^+_{(aq)} + 2H_2O_{(l)} \quad (9)$$

$$3Se_{(s,\ bulk)} + 2Sb_{(s,\ bulk)} \rightleftharpoons Sb_2Se_{3(s)} \quad (10)$$

After deposition, the films were submitted to TT at different times and temperatures. These films were physically and photoelectrochemically characterized in order to obtain insight into the effects of this treatment on optoelectronic quality and photoactivity toward hydrogen gas generation (from water splitting) of the electrodeposited Sb_2Se_3 thin films.

2.2. Physical Characterization

First of all, the surface morphology of the electrodeposited films was examined by SEM and the micrographs are shown in Figure 5 for various temperatures and TT durations. It was visually observed that the thickness of the films submitted to TT at 400 °C for 6 h and 500 °C for 1 h was drastically decreased under these conditions. This effect was probably caused by films sublimation and therefore, their data will not be presented here.

From Figure 5, we can see that the TT did not significantly change the film morphology. All the surfaces were quite rough, uniform, homogeneous and presented a globular-like shape independent of the TT conditions. In sequence, the phase and unit cell parameters, band gap, and composition of the films were evaluated by XRD, NIR-UV-vis spectroscopy and EDX, respectively. The data from these analyses were organized in

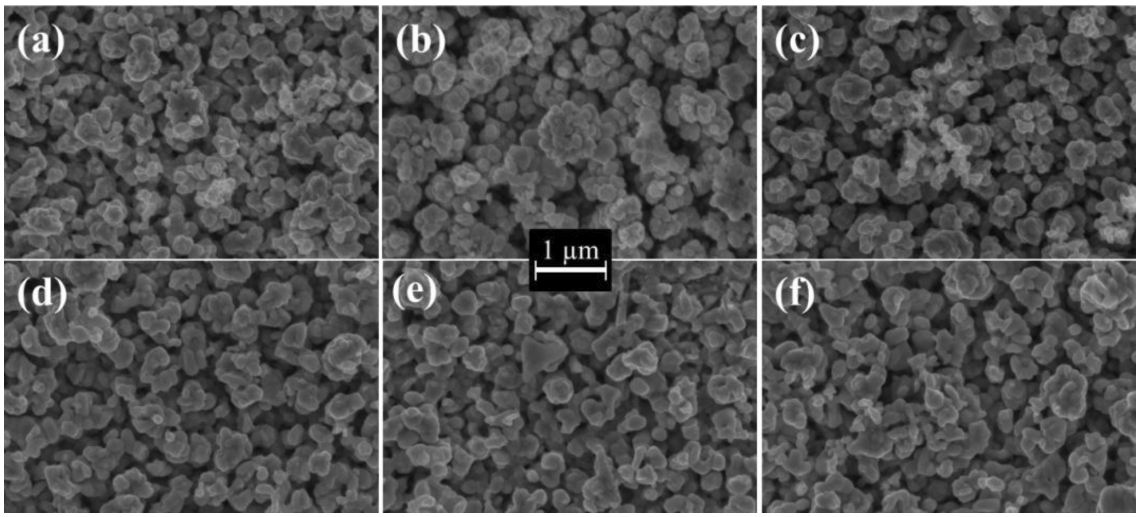

Figure 5. SEM images of the thin film surfaces submitted to different conditions of thermal treatment: a) non-treated; b) 300 °C for 1 h; c) 300 °C for 3 h; d) 300 °C for 6 h; e) 400 °C for 1 h; and f) 400 °C for 3 h.

Table 1, and the XRD patterns and the graph of $(\alpha h\nu)^2$ vs. photon energy are, respectively, shown in Figures 6 and 7.

As can be seen in Figure 6, all peaks could be associated to the orthorhombic phase of Sb_2Se_3 (JCPDF 89-821) or to the

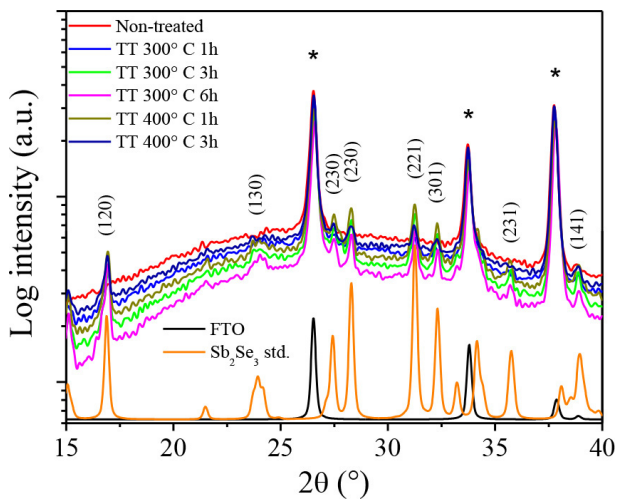

Figure 6. XRD patterns (intensity on logarithmic scale) of the thin films submitted to different thermal treatment conditions. The standard SnO_2 (representing FTO, JCPDF 77-451) and Sb_2Se_3 (JCPDF 89-821) diffraction patterns are shown in the lower region of the graph for comparison.

substrate (SnO_2, ascribed by the symbol "*", JCPDF 77-451).[43] Thus, we can conclude that all thermal-treated films presented a single phase; the logarithmic scale helped us to verify the presence of any secondary phases. The sample with no TT, as expected, did not show diffraction peaks related to the Sb_2Se_3 phase, meaning that this film was amorphous or nanocrystalline. This film was labeled as "non-treated". From the analysis of the XRD patterns, we could obtain the unit cell parameters and relative texture coefficient (TC_{Rel}) related to the ratio between the intensities of the (221) and (120) planes in comparison to the same ratio from standard non-texturized Sb_2Se_3 (JCPDF 89-821). This comparison was made by Eq. (11) and the data are organized in Table 1 for each film.

$$TC_{Rel} = \frac{I(221)_{Film}/I(120)_{Film}}{I(221)_{Std}/I(120)_{Std}} \quad (11)$$

According to Jiang Tang and collaborators,[28] the Sb_2Se_3 has 1D crystal structure composed by $(Sb_4Se_6)_n$ ribbons that are formed along the [001] direction by covalent bonds. In turn, these ribbons are stacked along the [100] and [010] directions by van der Waals forces. Thus, any crystallographic texturization that favors the [001] direction in front of the [100] and [010] directions, also favors the charge transport parallel to the substrate's normal vector; the former charge carriers travel within the covalent bonds of the ribbons is easier than their travel by jumping between ribbons. In our case, from the planes observed in the XRD patterns of Figure 6, the ratio between the texture coeficient of the (221) and (120) planes is a good manner to verify the favoring of the [001] direction; thus, as greater is this ratio, greater is the contribution of the [001] direction and better will be the charge transport parallel to the substrate's normal vector.

Finally, Figure 7 shows the curve $(\alpha h\nu)^2$ vs. photon energy ($h\nu$) in a range of 0.69 to 1.55 eV. The linear extrapolation of the curve to $(\alpha h\nu)^2 = 0$ shows that the band gaps of the treated samples were around 1.1 (as can be seen in Table 1), which correspond to the band gap values reported in the literature.[25,37,44] The non-treated film did not show a defined response, which agrees with the fact that this film is poorly crystalline.

As can be seen in Table 1, the as-deposited (non-treated) film was slightly Sb-rich and all TT films had a composition really close to stoichiometric Sb_2Se_3. From this EDX analysis, we could conclude that the TT promoted not only an increase in

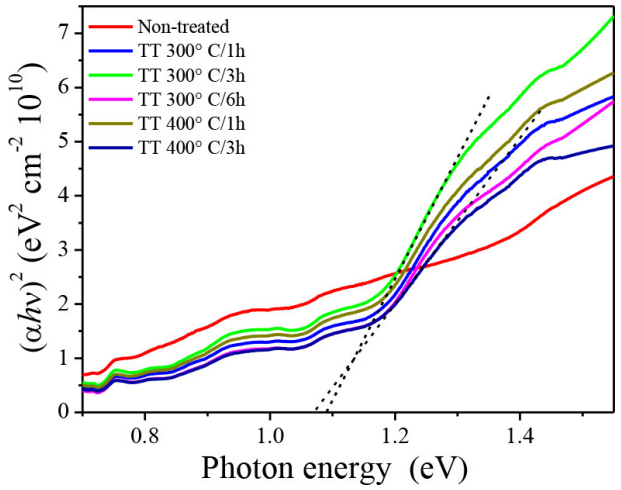

Figure 7. Plot of $(\alpha h\nu)^2$ vs. photon energy. The value of the linear extrapolation at the *x*-axis is equal to the band gap (E_g).

2.3. Photoelectrochemical Characterization

The photoelectrochemical tests were evaluated by linear voltammetry in the dark and under light, and photocurrent transient (Figures 8A and B, respectively), with the photocurrent values organized in Table 2. The scans were performed from the open circuit potential of each film in the dark, toward more negative potentials, to −0.4 V vs. Ag/AgCl/Cl$^-_{(KCl\ sat)}$, potential 85.0 mV more negative than the reduction of H^+ at pH 2 (−0.315 V). The transient of the photocurrent was collected right at the standard hydrogen proton reduction potential. To visualize the effect of the crystallographic texture on the photocurrent of the films, the Figure 8C shows the graph of relative texture coefficient, for the ratio between the (221) and (120) planes, versus photocurrent intensities.

Table 2. Photocurrent intensity for electrodeposited films submitted to different thermal treatment conditions.[a]

Sample	Current density [μA cm^{-2}] (μA cm^{-2})*
non-treated	91.49
TT 300 °C/1 h	148.50
TT 300 °C/3 h	168.15
TT 300 °C/6 h	58.27
TT 400 °C/1 h	124.82
TT 400 °C/3 h	20.10

[a] At −0.315 V vs. Ag/AgCl/Cl$^-_{(sat.\ KCl)}$ and in 0.5 M Na_2SO_4/H_2SO_4 at pH 2; standard deviation ($n=3$) was lower than 8%, with 95% confidence.

the film crystallinity (already seen from XRD data), but also the adjustment of the elemental composition, important parameters for achieving good photoelectroactivity and optoelectronic properties.

From the TC_{Rel} values, we can see that the TT 300 °C/3 h and TT 400 °C/1 h were almost non-texturized while, the TT 300 °C/1 h and TT 400 °C/3 h were the most texturized in the [120] direction. Additionally, comparing the crystallographic parameters of the films with those from standard Sb_2Se_3 (JCPDF 89-821),[43] we observed, that despite a good match between each parameter, the TT 400 °C/3 h and TT 300 °C/1 h films were those that showed unit cell volumes more different than the standard, which may be correlated to a higher crystallographic stress for these films. This stress could be caused by the high degree of texturization that distorted the unit cell during the growth and crystallization. Thus, it is expected that this texturization in the [120] direction as well as this slightly higher crystallographic stress make these films have the worst charge transport compared to the others.

In order to study how these different TT conditions and physical characteristics affect the photoactivity of the films, they were photoelectrochemically characterized toward hydrogen proton reduction.

In both graphs of Figure 8A and B, we observed a cathodic photocurrent, which is characteristic of a p-type semiconductor. In Figure 8A, we can see that the higher photoactivity is achieved for the TT 300 °C/3 h film, which also showed different electrochemical behavior. This higher photocurrent can be correlated not only to a better photoactivity toward hydrogen gas production, but also to higher solar cell efficiency if a photovoltaic device is constructed with this film, as demonstrated by Colombara et al.[45] for Cu(In,Ga)Se_2 thin films. In addition, this different electrochemical behavior seems to be a saturation phenomenon that can be associated to a charge transfer limiting at this potential range, and because of this, the photon generated charges are trapped at the electrode surface and may cause film damage (by photoreduction) at more negative potentials. From this discussion, we can argue that one way to improve the photoactivity of this film is by using a

Table 1. Composition, band gap and unit cell parameters for the electrodeposited Sb_2Se_3 films submitted to different thermal treatment conditions.

Sample	Composition [% at.][a]		E_g [eV]	TC_{Rel}[b]	Unit cell parameters			
	Sb	Se			*a* [Å]	*b* [Å]	*c* [Å]	*V* [Å^3]
non-treated	47.0	53.0	–	–	–	–	–	–
TT 300 °C/1 h	40.8	59.2	1.08	0.55	11.60	11.72	3.98	540.95
TT 300 °C/3 h	39.9	60.1	1.09	1.15	11.56	11.74	3.97	539.13
TT 300 °C/6 h	39.6	60.4	1.09	0.70	11.58	11.75	3.97	539.52
TT 400 °C/1 h	40.4	59.6	1.08	0.93	11.58	11.74	3.97	540.10
TT 400 °C/3 h	39.8	60.2	1.07	0.48	11.59	11.75	3.97	540.81
JCPDF 89-821	–	–	–	1	11.59	11.74	3.95	538.23

[a] Standard deviation ($n=3$) was lower than 5%, with 95% confidence. [b] Texture coefficient for the ratio between the (221) and (120) planes.

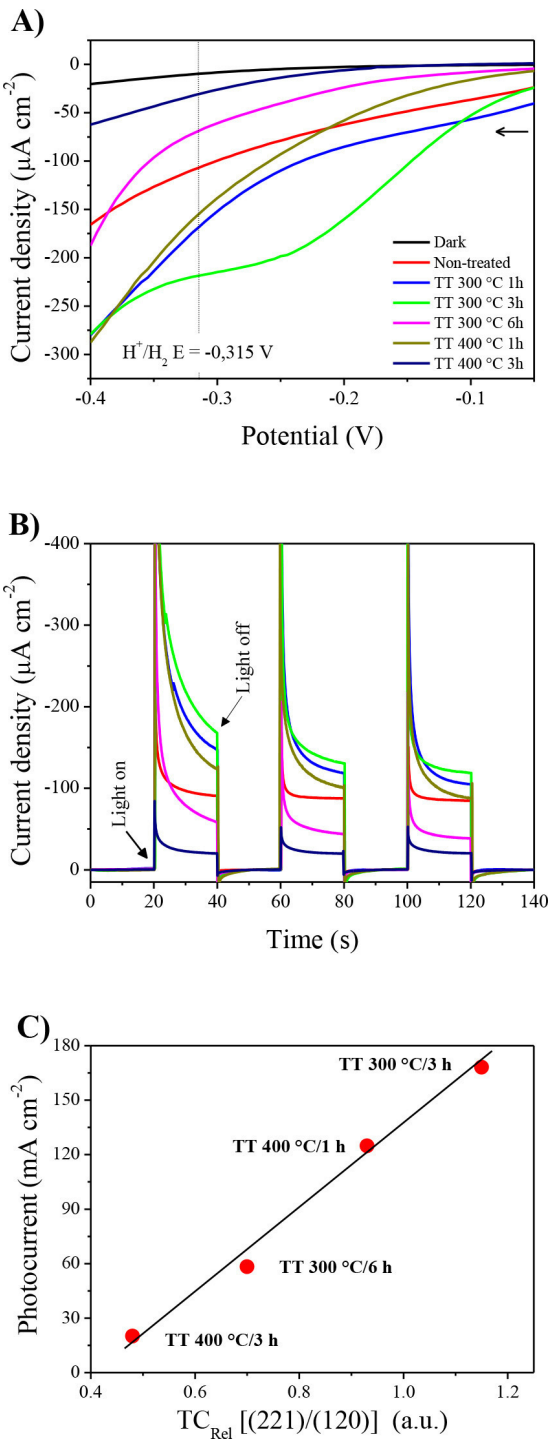

Figure 8. A) Linear voltammograms at a scan rate of 50 mV s^{-1} in the dark and under solar simulated illumination (1 sun, 100 mW cm^{-2}, lens A.M. 1.0) and B) photocurrent transient at the standard hydrogen reduction potential, −0.315 V vs. Ag/AgCl/$Cl^-_{(sat.\ KCl)}$, for Sb_2Se_3 films submitted to different conditions of thermal treatment. C) Graph of relative texture coefficient, for the ratio between the (221) and (120) planes, versus photocurrent intensities.

charge transfer catalyst on the surface, such as platinum nanoparticles.

In Table 2, we can observe the mean values of the films photocurrent, concluding that the optimized TT condition was achieved at 300 °C for 3 h. It is worth mentioning that, as far as we know, the higher photocurrent for hydrogen gas production in acid medium previous reported for this material was 50 μA cm^{-2}[25] (three times lower than in this work). We can also see that the films treated for longer times (6 h at 300 °C or 3 h at 400 °C) showed lower photocurrents. This phenomenon can be correlated to the increase of electronic defects or crystallographic disorder, which, in both cases, did not significantly affect the composition of the films. Beyond this, the texturization in the [120] direction can also explain these lower photocurrents. From Figure 8C, we can clearly observe a linear behavior between the texture coefficients and the photocurrents, proving that, in this case, the crystallographic texturization is one of the parameters that most affected the photocurrent of these films. It is worth to mention that the TT 300 °C/1 h film showed photocurrent higher than expected (based on its texture) and was not showed in this graph. This result indicates that for this film, besides the texture, there could be another factor related to the photocurrent response. One would be the quality of the film, however further investigation would be needed.

Summarizing the whole results and discussion, we can conclude that TT at higher temperatures and longer times promote the texturization of the film in the [120] direction, which is detrimental to its charge transport and, by consequence, photoactivity. Calculations performed by Ying Zhou and coauthors[28] revealed that the (120) surface is one of the surfaces with the lowest formation energies and this can explain the observed crystallographic texturization. For future studies, we think that in order to increase the texturization of the electrodeposited films in the [221] or [001] direction (less energetically favorable texturization), these films can be grown by electrochemical atomic layer epitaxy (ECALE), an electrochemical method equivalent of atomic layer epitaxy (ALE), and treated by rapid thermal anneal (RTA) under same atmosphere used in this work.

3. Conclusions

The behavior of electrodeposited Sb_2Se_3 thin films on FTO in different TT conditions was investigated. Generally, the morphology of the films showed no significant changes, with high surface roughness, uniformity and homogeneity as well as a globular shape in all conditions. With respect to the crystallinity, the peaks associated to the orthorhombic phase of Sb_2Se_3 were demonstrated with some crystallographic texturing. The TT also contributed to the setting of a more stoichiometric elemental composition than the untreated sample. The band gaps of the treated films were in accordance with those reported in the literature, with values near 1.1 eV. We noted that in the photoelectrochemical experiment, a large influence of the TT on the photoactivity of the films occurred, in which the sample treated at 300 °C for 3 h obtained the highest photocurrent of 168.15 μA cm^{-2}. It was observed that crystallographic stress and texturization can be detrimental to the photoactivity of this material. In other words, the phase pure Sb_2Se_3 treated thin film

has good optoelectronic properties and photoactivity toward hydrogen gas production and can be grown by electrodeposition, which is a non-vacuum, fast, easy and cheap method.

Acknowledgments

This work was supported by National Counsel of Technological and Scientific Development (CNPq) and the São Paulo Research Foundation (FAPESP), grant #2016/10513-3, and CEPID grant #2013/07296-2.

Conflict of Interest

The authors declare no conflict of interest.

Keywords: antimony selenide · photoelectrochemistry · water splitting · electrodeposition · one-dimensional $(Sb_4Se_6)_n$ ribbons

[1] K. E. Trenberth, J. T. Fasullo, J. Kiehl, *Bull. Am. Meteorol. Soc.* **2009**, *90*, 311–323.
[2] O. Edenhofer, R. Pichs-Madruga, Y. Sokona, K. Seyboth, P. Eickemeier, P. Matschoss, G. Hansen, S. Kadner, S. Schlömer, T. Zwickel, et al., *Renewable Energy Sources and Climate Change Mitigation: Summary for Policymakers and Technical Sumary*, **2011**.
[3] C. A. Wolden, J. Kurtin, J. B. Baxter, I. Repins, S. E. Shaheen, J. T. Torvik, A. A. Rockett, V. M. Fthenakis, E. S. Aydil, *J. Vac. Sci. Technol. A Vacuum, Surfaces Film.* **2011**, *29*, 30801.
[4] M. I. Hoffert, K. Caldeira, A. K. Jain, E. F. Haites, L. D. D. Harvey, S. D. Potter, M. E. Schlesinger, S. H. Schneider, R. G. Watts, T. M. L. Wigley, et al., *Nature* **1998**, *395*, 881–884.
[5] F. Dross, K. Baert, T. Bearda, J. Deckers, V. Depauw, O. El Daif, I. Gordon, A. Gougam, J. Govaerts, S. Granata, et al., *Prog. Photovoltaics Res. Appl.* **2012**, *20*, 770–784.
[6] F. W. S. Lucas, A. R. F. Lima, L. H. Mascaro, *RSC Adv.* **2015**, *5*, 18295–18300.
[7] F. W. de S. Lucas, A. R. F. Lima, L. H. Mascaro, *Electrochim. Acta* **2014**, *147*, 47–53.
[8] Research Cell Efficiency Records. Available at: *http//www.nrel.gov/ncpv/images/efficiency_chart.jpg.* Last accessed date was January/2015.
[9] M. F. Gromboni, F. W. S. Lucas, L. H. Mascaro, *J. Braz. Chem. Soc.* **2014**, *23*, 526–531.
[10] C. Wadia, A. P. Alivisatos, D. M. Kammen, *Environ. Sci. Technol.* **2009**, *43*, 2072–2077.
[11] K. Ramasamy, M. A. Malik, P. O'Brien, *Chem. Sci.* **2011**, *2*, 1170–1772.
[12] V. Itthibenchapong, R. S. Kokenyesi, A. J. Ritenour, L. N. Zakharov, S. W. Boettcher, J. F. Wager, D. A. Keszler, *J. Mater. Chem. C* **2013**, *1*, 657–662.
[13] A. Kanai, H. Araki, A. Takeuchi, H. Katagiri, *Phys. status solidi* **2015**, *252*, 1239–1243.
[14] B. Yang, L. Wang, J. Han, Y. Zhou, H. Song, S. Chen, J. Zhong, L. Lv, D. Niu, J. Tang, *Chem. Mater.* **2014**, *26*, 3135–3143.
[15] A. Zakutayev, L. L. Baranowski, A. W. Welch, C. A. Wolden, E. S. Toberer, *2014 IEEE 40th Photovolt. Spec. Conf.*, IEEE, **2014**, 2436–2438.
[16] F. W. de Souza Lucas, A. W. Welch, L. L. Baranowski, P. C. Dippo, L. H. Mascaro, A. Zakutayev, *2015 IEEE 42nd Photovolt. Spec. Conf.*, IEEE, **2015**, 1–5.
[17] A. W. Welch, L. L. Baranowski, F. W. de Souza Lucas, E. S. Toberer, C. A. Wolden, A. Zakutayev, *2015 IEEE 42nd Photovolt. Spec. Conf.*, IEEE, **2015**, 1–4.
[18] F. W. de Souza Lucas, A. W. Welch, L. L. Baranowski, P. C. Dippo, H. Hempel, T. Unold, R. Eichberger, B. Blank, U. Rau, L. H. Mascaro, et al., *J. Phys. Chem. C* **2016**, *120*, 18377–18385.
[19] Y. C. Choi, T. N. Mandal, W. S. Yang, Y. H. Lee, S. H. Im, J. H. Noh, S. Il Seok, *Angew. Chem., Int.* **2013**, *126*, 1353–1357.
[20] X. Ding-Jiang, S. Hang-Jie, T. Jiang, *Acta Phys. Sin.-Chinese Ed.* **2015**, *64*, 38406.
[21] T. T. Ngo, S. Chavhan, I. Kosta, O. Miguel, H.-J. J. Grande, R. R. Tena-Zaera, *ACS Appl. Mater. Interfaces* **2014**, *6*, 2836–2841.
[22] Y. Rodríguez-Lazcano, Y. Pena, M. T. S. Nair, P. K. Nair, *Thin Solid Films* **2005**, *493*, 77–82.
[23] S. Messina, M. T. S. Nair, P. K. Nair, *J. Electrochem. Soc.* **2009**, *156*, H327–H332.
[24] W. Shockley, H. J. Queisser, *J. Appl. Phys.* **1961**, *32*, 510–519.
[25] Y. Lai, Z. Chen, C. Han, L. Jiang, F. Liu, J. Li, Y. Liu, *Appl. Surf. Sci.* **2012**, *261*, 510–514.
[26] M. Luo, M. Leng, X. Liu, J. Chen, C. Chen, S. Qin, J. Tang, *Appl. Phys. Lett.* **2014**, *104*.
[27] O. Madelung, Semiconductors: Group IV Elements and III–V Compounds,Vol. 1, Springer-Verlag, Berlin, **1992**.
[28] Y. Zhou, L. Wang, S. Chen, S. Qin, X. Liu, J. Chen, D. Xue, M. Luo, Y. Cao, Y. Cheng, et al., *Nat. Photonics* **2015**, *9*, 409–415.
[29] W. Liu, S. Hsieh, W. Chen, P. Wei, J. Lee, *Int. J. Miner. Metall. Mater.* **2009**, *16*, 101–107.
[30] N. Abdul-Manaf, H. Salim, M. Madugu, O. Olusola, I. Dharmadasa, *Energies* **2015**, *8*, 10883–10903.
[31] A. Y. Shenouda, E. S. M. El Sayed, *Ain Shams Eng. J.* **2015**, *6*, 341–346.
[32] A. K. Turner, J. M. Woodcock, M. E. Özsan, D. W. Cunningham, D. R. Johnson, R. J. Marshall, N. B. Mason, S. Oktik, M. H. Patterson, S. J. Ransome, *Sol. Energy Mater. Sol. Cells* **1994**, *35*, 263–270.
[33] D. Lincot, J. F. Guillemoles, S. Taunier, D. Guimard, J. Sicx-Kurdi, A. Chaumont, O. Roussel, O. Ramdani, C. Hubert, J. P. Fauvarque, et al., *Sol. Energy* **2004**, *77*, 725–737.
[34] S. Taunier, J. Sicx-Kurdi, P. P. Grand, A. Chomont, O. Ramdani, L. Parissi, P. Panheleux, N. Naghavi, C. Hubert, M. Ben-Farah, et al., *Thin Solid Films* **2005**, *480–481*, 526–531.
[35] J.-O. Jeon, K. D. Lee, L. Seul Oh, S.-W. Seo, D.-K. Lee, H. Kim, J. Jeong, M. J. Ko, B. Kim, H. J. Son, et al., *ChemSusChem* **2014**, *7*, 1073–1077.
[36] L. M. Peter, *Electrochem. commun.* **2015**, *50*, 88–92.
[37] Y. Lai, C. Han, X. Lv, J. Yang, F. Liu, J. Li, Y. Liu, *J. Electroanal. Chem.* **2012**, *671*, 73–79.
[38] M. C. Santos, S. a. S. Machado, *J. Electroanal. Chem.* **2004**, *567*, 203–210.
[39] A. Tang, M. Long, Z. He, *Electrochim. Acta* **2014**, *146*, 346–352.
[40] J. Yang, W. Zhu, X. Gao, S. Bao, X. Fan, X. Duan, J. Hou, *J. Phys. Chem* **2006**, *2*, 4599–4604.
[41] Y. Chen, L. Wang, A. Pradel, A. Merlen, M. Ribes, M. C. Record, *J. Solid State Electrochem.* **2015**, 19, 2399–2411.
[42] A. Fernández, M. Merino, *Thin Solid Films* **2000**, *366*, 202–206.
[43] Inorganic Crystal Structure Database. Available at: <*http://www.fiz-karlsruhe.de/icsd.html*>. Last accessed date was May/2017.
[44] A. P. Torane, K. Y. Rajpure, C. H. Bhosale, *Mater. Chem. Phys.* **1999**, *61*, 219–222.
[45] D. Colombara, A. Crossay, D. Regesch, C. Broussillou, T. G. de Monsabert, P.-P. Grand, P. J. Dale, *Electrochem. commun.* **2014**, *48*, 99–102.

Manuscript received: May 24, 2017
Accepted Article published: June 23, 2017
Version of record online: July 11, 2017